AIAA Journal
Vol. 45, No. 8, August 2007

Family of Micromachined Wall Hot-Wire Sensors on Polyimide Foil

Ulrich Buder,* Andreas Berns,† Jan-Philipp von Klitzing,‡ and Ernst Obermeier§
Technical University of Berlin, 13355 Berlin, Germany
and
Ralf Petz¶ and Wolfgang Nitsche**
Technical University of Berlin, 10587 Berlin, Germany

DOI: 10.2514/1.25033

Micromachined wall hot-wire sensors composed of a highly sensitive, nickel, thin-film resistor spanning an air-filled cavity in a mechanically flexible substrate are presented. Cavity design and sensor materials are optimized to reduce thermal losses, thus enabling measurement of high-frequency fluctuations in fluid flows. Successfully realized sensors featuring wire widths of 2 and 5 μm, wire lengths from 400 to 2000 μm, and various cavity dimensions were characterized in wind-tunnel experiments. Static sensor calibration, cutoff frequency determination using a sine sweep, and recording of angular characteristics were conducted at wall shear stresses of up to 1 $\mathrm{N/m^2}$, obtained at 20 m/s freestream velocity in an open wind tunnel on a flat plate with fully developed turbulent flow. An overheat ratio of 1.8 was used for hours without thermal failure of the sensors, and a maximum cutoff frequency in still air of 73 kHz was obtained. The highest average sensitivity of 0.196 $\mathrm{V/(N/m^2)}$ was recorded for a sensor of 5-μm wire width and a length-to-width ratio of 400 in a wall shear stress range from 0 to 1 $\mathrm{N/m^2}$ with a power consumption of less than 30 mW.

Nomenclature

a_W = overheat ratio of the hot wire
d_C = depth of the cavity, μm
k = yaw factor
l_C = length of the cavity, μm
l_W = length of the hot wire, μm
P = electrical power consumption, W
R_W = electrical resistance of the hot wire in operation, Ω
R_0 = electrical resistance of the hot wire at room temperature, Ω
S_τ = sensitivity of the sensor to changes in wall shear stress, $\mathrm{V/(N/m^2)}$
T_W = temperature of the heated wire, K
T_0 = ambient fluid temperature, K
t_F = thickness of the polyimide foil, μm
t_W = thickness of the hot wire, μm
U = anemometer output voltage with flow in constant-temperature operation, V
U_0 = anemometer output voltage without flow in constant-temperature operation, V
U_{0° = anemometer output voltage with flow normal to the wire length in constant-temperature operation, V
v = flow velocity at the hot wire, m/s
v_{eff} = flow velocity contributing to cooling of the hot wire, m/s
v_n = component of flow velocity normal to the hot-wire length, m/s
v_∞ = freestream velocity, m/s
w_C = width of the cavity, μm
w_W = width of the hot wire, μm
θ = yaw angle, deg
τ = wall shear stress, $\mathrm{N/m^2}$

I. Introduction

Precise characterization of the state of wallbound flows occurring on surfaces of a multitude of technical objects used in aerospace transportation (e.g., airplane airfoils and fuselages), Earthbound transportation of passengers (e.g., car bodies) and goods (e.g., pipe flows), or in power generation (e.g., turbine blades) relies on knowledge of temporal and spatial distributions of wall shear stress and its fluctuations [1]. Based on experimentally obtained information, the prediction of important flow phenomena such as transition or separation is possible and systems for active flow control can be developed and employed. Active control of transition, separation, noise, and skin friction drag will contribute to air travel safety, environmental compatibility, and airplane efficiency [2]. Investigating the effect of drag reduction through active control of wallbound flows on airplanes alone, annual cost reductions of billions of dollars in fuel are estimated [3].

Sensors detecting wall shear stress are either direct-measurement-based devices using floating elements or make use of indirect measurement principles relying on heat transfer phenomena [1,4], correlation methods [1], or momentum balance [1]. Production of the former is usually complex and thus expensive; sensor dimensions are large and miniaturization reduces sensor durability. Indirectly measuring sensors, predominantly hot wires and hot films, are comparatively easy to manufacture and can be miniaturized without necessarily affecting durability. For measurement of wall shear stress in turbulent flows, sensor miniaturization is highly important because flow features as small as 100 μm within timescales of 2 ms or less can occur in low-speed turbulent boundary layers [5]. To reduce overall sensor size beyond dimensions realizable with conventional machining technology or precision engineering, to

---

Presented as Paper 1244 at the 44th AIAA Aerospace Sciences Meeting and Exhibit, Reno, NV, 9–12 January 2006; received 8 May 2006; revision received 16 February 2007; accepted for publication 6 March 2007.

*Ph.D. Student, Microsensor and Actuator Technology Center, Gustav-Meyer-Allee 25. Member AIAA.

†Ph.D. Student, Microsensor and Actuator Technology Center, Gustav-Meyer-Allee 25.

‡Graduate Student, Microsensor and Actuator Technology Center, Gustav-Meyer-Allee 25.

§Professor, Microsensor and Actuator Technology Center, Gustav-Meyer-Allee 25.

¶Ph.D. Student, Institute of Aeronautics and Astronautics, Department of Aerodynamics, Marchstraße 12. Member AIAA.

**Professor, Institute of Aeronautics and Astronautics, Department of Aerodynamics, Marchstraße 12.

lower production costs, and to simplify production processes, microelectromechanical systems (MEMS) technology is widely used in manufacturing miniature flow sensors for research applications. A variety of MEMS flow sensors employing direct or indirect measuring principles exists [6], some of which allow for measurement of turbulent fluctuations up to 50 kHz and beyond [7].

Although the temporal resolution of selected MEMS and conventional wall shear stress sensors is sufficient for monitoring of fluctuations in wallbound flows, the problem of providing both a high spatial and a high temporal resolution using one shear-stress sensor system has only received limited attention. Hot-film arrays based on flexible printed circuit boards (flex PCBs) and arrays of manually assembled wall hot wires have been realized and successfully employed to detect Tollmien–Schlichting instabilities before transition [8], reattachment behind a backward-facing step [9], and wall shear stress distributions on the surface of a cylinder in air flow [10]. Combined with miniature actuators, closed-loop control reducing undesirable flow effects is possible.

Almost all MEMS sensors used for wall shear stress measurement today are silicon-based, due to the predominant role of the material in semiconductor and MEMS processing [11]. Arrays of micromachined thermal wall shear stress sensors on a rigid silicon substrate have enabled researchers to conduct measurements on flat plates [12]. The use of such silicon-based sensors or sensor arrays on curved surfaces inevitably results in boundary-layer disturbances caused by the thickness of the silicon sensors and the distortion of the original surface contour. Efforts to reduce this distortion make use of small rigid silicon chips embedded into a mechanically flexible polyimide (PI) layer [13] to provide semiflexible wall shear stress sensor arrays [14]. Thus, a reduction of the mismatch in curvature is possible. Still, both bending radius and reproducibility of the original surface shape are limited by the size of the silicon islands (Fig. 1).

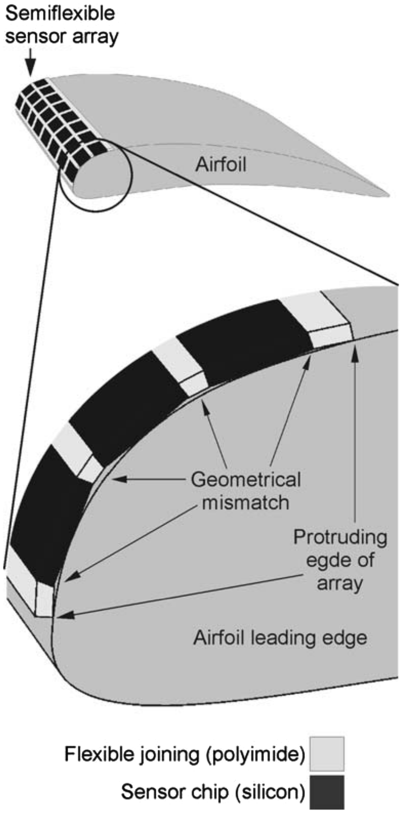

Fig. 1 Geometrical mismatch of a silicon-based semiflexible sensor array and aerodynamic surface.

Power consumption and temporal behavior of a hot wire at a fixed overheat ratio are dependent on thermal losses of the wire to its surroundings. Materials with low thermal conductivity and heat capacity induce low power consumption and small time constants for heating and cooling of the wire. It is noteworthy that almost all MEMS wall hot wires presented in literature make use of structures directly coupled to the wire over its full length. Membranes, beams, or bridges [15,16] (depicted in Fig. 2) are most commonly used to provide mechanical support for the wire or to ease production processes. Such structures also influence the thermal equilibrium of the wire and thus have direct influence on the power consumption and temporal behavior of the sensor.

The family of sensors introduced herein is the building block for a measurement system that allows for monitoring of wall shear stress and its spatial and temporal fluctuations. All sensors presented here feature a fully flexible substrate material to avoid mechanical mismatch of sensor and measurement surface, as well as small metallic hot wires with a very high temperature coefficient of resistance (TCR). Power consumption and temporal behavior of the sensors were optimized by thermal simulation, through careful material selection, omitting of supporting structures for the hot wires, and the introduction of an air-filled cavity underneath the wire.

II. Sensor Design, Optimization, and Fabrication

A. Basic Sensor Setup

A three-dimensional schematic of the basic setup of the MEMS hot-wire sensors presented here is given in Fig. 3. Unlike the sensors depicted in Fig. 2, no mechanical structure is directly coupled to the hot wire. An air-filled cavity thermally insulates the heated element and enables the flow to fully surround the wire. At the cavity edges, the 2-μm-thick and 2- or 5-μm-wide hot wire merges with 50-μm-wide conducting paths. Because Joule heat generation is small in the conducting paths, unwanted heat losses mainly occur through heat conduction from the hot wire over the conducting paths into the substrate.

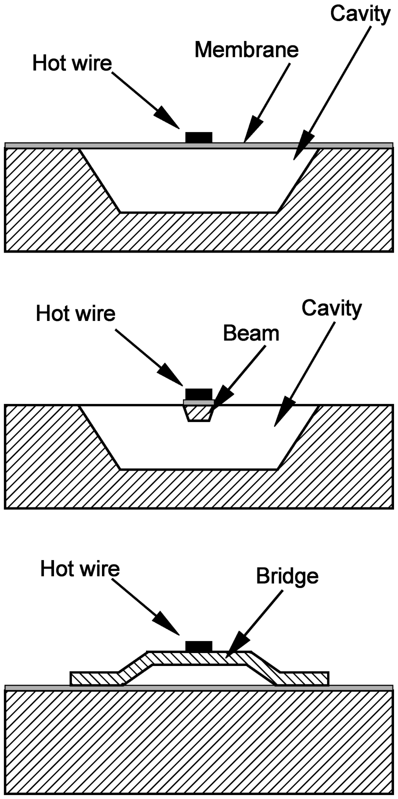

Fig. 2 Structures directly coupled to MEMS wall hot wires on silicon.

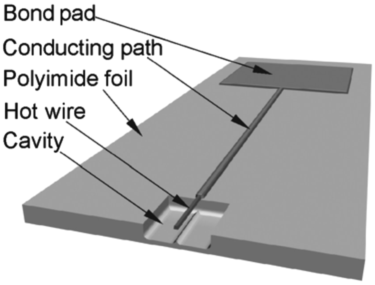

Fig. 3 Three-dimensional schematic of half of a hot-wire sensor on polyimide foil.

B. Material Selection

To allow for application of the sensor to aerodynamic surfaces, a flexible substrate material is needed. Polyimide foil, available from different suppliers, has proven compatible with microelectronic processing and, at present, is the most important substrate material for flex PCBs [17]. Polyimide is very resistant to chemical attack and, in the group of polymers, has a very high maximum operating temperature of almost 400°C. Its thermal conductivity is very low ($0.147\ \mathrm{W \cdot m^{-1} \cdot K^{-1}}$) [18] compared with the average conductivity of silicon ($156\ \mathrm{W \cdot m^{-1} \cdot K^{-1}}$ at 300 K) [19] or thin-film silicon nitride ($4.5\ \mathrm{W \cdot m^{-1} \cdot K^{-1}}$) [20]. Silicon nitride is employed as the membrane material in MEMS wall hot wires on a supporting membrane over a sealed low-pressure cavity [12,21]. For the realization of a cavity underneath the hot wire, structuring of the substrate material using MEMS processes is necessary. A specific polyimide that is processable by reactive-ion etching (RIE) at sufficiently high etch rates was identified [22].

Careful selection of the hot-wire material is necessary because at a given overheat ratio, which is defined as the quotient of the hot-wire temperature in operation and the ambient fluid temperature, the TCR of the material dominates the sensitivity of the sensor to wall shear stress fluctuations. Doped polysilicon, as used in many silicon-based micromachined wall hot wires, exhibits a TCR in the range from 0.0008 to 0.003 $\mathrm{K^{-1}}$ [23], but, dependent on doping concentration, has a substantial piezoresistive effect when subjected to mechanical stresses (e.g., membrane bending due to pressure differences). Metals can exhibit even higher temperature coefficients of resistance than doped polysilicon, with nickel featuring one of the highest known bulk TCR (0.0068 $\mathrm{K^{-1}}$) of a metal [24] that can be deposited by MEMS processes. Thin-film metals usually have a lower TCR than bulk metals; however, a TCR for thin-film nickel of 0.0055 $\mathrm{K^{-1}}$ has been reported [25], and therefore nickel is selected as the wire material.

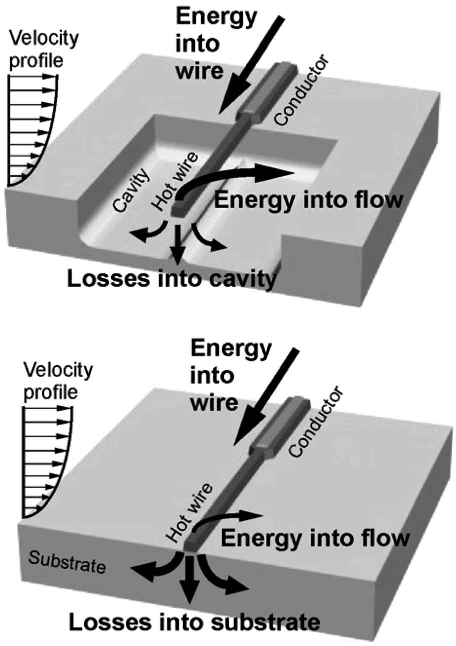

Fig. 4 Energy balance of a wall hot-wire sensor with a cavity (top) and a wall hot wire without a cavity (bottom).

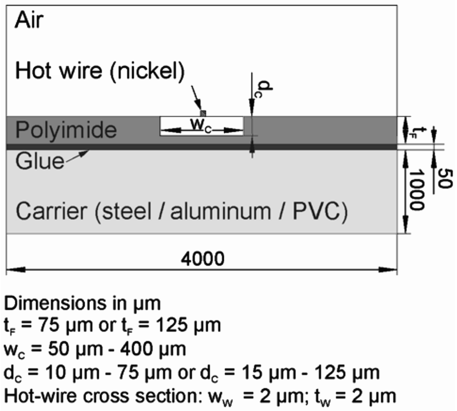

Fig. 5 Model of a cross section of a MEMS wall hot wire with a cavity for thermal FEM simulation.

C. Thermal Optimization

To thermally optimize the sensor design, a series of two- and three-dimensional thermal finite element method (FEM) simulations are performed. The primary objective of the optimization is the reduction of thermal conduction into substrate and metal paths. Figure 4 schematically depicts the energy balance of a wall hot wire with and without a cavity. Keeping in mind that air has a thermal conductivity of approximately one-fifth of that of polyimide, it is immediately obvious that an air-filled cavity underneath the hot wire induces low thermal losses into the substrate. Supplying the same amount of electrical power to a wall hot wire with and without a cavity, the equilibrium temperature in the hot wire over the cavity will be higher, inducing a higher cutoff frequency and an increase in sensitivity to wall shear stress fluctuations. In consequence, the wall hot-wire sensor with a cavity consumes less electrical power than the sensor without a cavity to heat up to the same wire temperature (see Sec. IV. B). As can be anticipated from Fig. 4, the amount of power reduction is dependent on the length, width, and depth of the cavity. Cavity depth is limited by the thickness of the substrate material, which itself has an influence on thermal losses. Because most surfaces to which such a sensor will be applied are made from materials with high thermal conductivity (e.g., aluminum and steel), thick polyimide-substrate layers provide better thermal insulation than thin layers. To optimize the thermal insulation of a wall hot wire with a cavity from the substrate, influences of cavity dimensions, substrate thickness, and the material of the measurement surface (carrier material) need to be examined.

Figure 5 shows a sketch of the cross section of a wall hot-wire sensor used for two-dimensional thermal simulations. All input parameters and the range of values in which they were varied are provided. Hot-wire height and width in all two-dimensional simulations are 2 and 2 μm, respectively. An investigation of the influence of cavity length is not possible in this type of simulation. It is obvious that for best thermal insulation, the cavity should span the entire length of the hot wire; therefore, a variation of cavity length independent of hot-wire length is not necessary.

Based on thermal simulations of various sensor cross sections, graphical representations of the temperature distribution around the hot wire can be generated, Fig. 6 being a typical example for a specific combination of materials and geometry. Furthermore, the power transferred from the wire to its surrounding, which is equal to the electrical power fed into the wire, can be determined. To obtain comparable power values, the wires in all configurations simulated were heated to an excess temperature of 200 K.

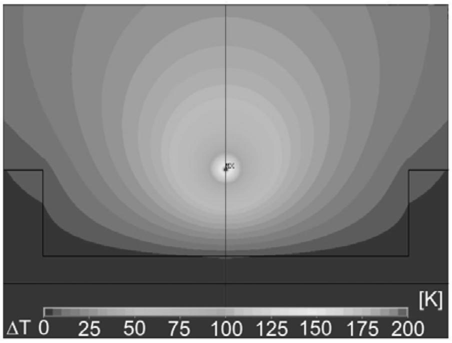

Fig. 6 Close-up of simulated temperature distribution around a hot wire and cavity.

The resulting power consumption of wall hot-wire sensors featuring various cavity geometries and two different polyimide thicknesses mounted to three different carrier materials is depicted in Figs. 7–9. Power-consumption values are provided for unity length of the hot wire, which equals 1 m. Because this simulation is based on a two-dimensional model, thermal conduction into conducting paths and other wire end effects cannot be included.

The overall level of simulated power consumption is primarily dependent on the thermal conductivity of the carrier material to which the sensor is attached. Polyvinyl chloride (PVC) has the lowest thermal conductivity of the carrier materials simulated, whereas aluminum and steel feature substantially higher values. Overall power consumption is therefore between 10 and 20% higher on steel and aluminum carriers than on a PVC carrier. As expected, a 125-μm-thick polyimide substrate insulates the hot wire better from the carrier materials than does a 75-μm-thick foil. This effect amounts to a maximum of approximately 13% in power reduction. Irrespective of differences in absolute values, changes in cavity dimensions bring about similar relative changes in power consumption on all carrier materials. An increase in cavity width from 50 to 400 μm with low cavity depth causes a reduction in power consumption of approximately 1.5 and 3% for polyimide-foil thicknesses of 75 and 125 μm, respectively. Changing cavity depth to values close to substrate thickness with a cavity width of 50 μm brings about an averaged change in power consumption of 15 and 9% for polyimide foil thicknesses of 75 and 125 μm, respectively. Combined enlargement of cavity width and depth to their maximum values is connected to a simulated electrical power reduction of more than 30% for both substrate thicknesses investigated. Because no end effects could be incorporated into this two-dimensional simulation, the power reduction in a fully optimized sensor featuring a 400-μm-wide and 100-μm-deep cavity in a 125-μm-thick polyimide substrate is expected to be higher than predicted here. In fact, the effectiveness of the cavity to thermally insulate the hot wire was also investigated experimentally and can be evaluated by comparing the measured power consumption of a sensor with and without a cavity. A reduction in the experimentally determined power consumption of approximately 60 and 70% is observed for overheat ratios of 1.2 and 1.8, respectively (see Sec. IV.B). In summary, two-dimensional simulations of the wall hot-wire sensor show that a 125-μm-thick polyimide substrate featuring a 100-μm-deep and 400-μm-wide cavity underneath the hot wire should be employed to minimize thermal losses. Therefore, all sensors investigated in this research (except the reference sensors, which feature hot wires directly coupled with the substrate mechanically and thermally) exhibit an air-filled cavity of 100-μm depth and at least 400-μm width.

Because thermal losses within a wall hot-wire sensor do not occur only by direct heat transfer from hot wire to substrate, power losses through Joule heating within and thermal conduction into the conducting paths should also be estimated. Because of the high thermal conductivity of nickel, it can be assumed that some thermal energy generated in the hot wires is lost into the conductors. At room temperature, the electrical resistance of a conducting path, dependent

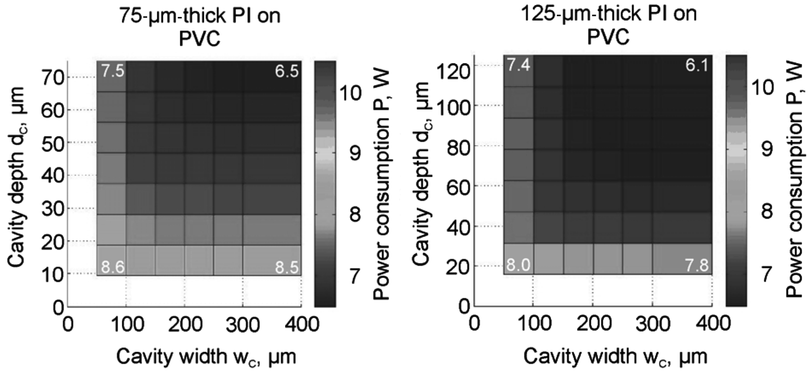

Fig. 7 Power consumption for a wall hot wire on PVC obtained from 2-D thermal simulation.

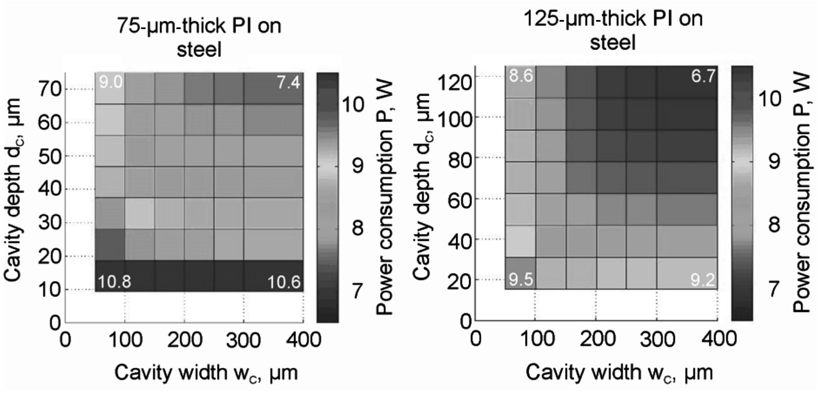

Fig. 8 Power consumption for a wall hot wire on steel obtained from 2-D thermal simulation.

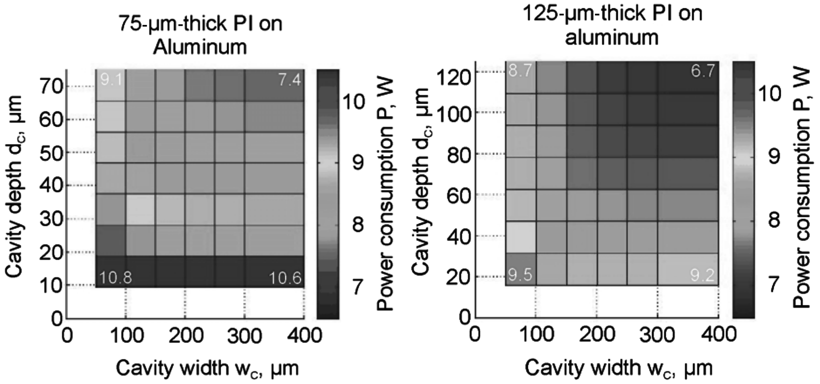

Fig. 9 Power consumption for a wall hot wire on aluminum obtained from 2-D thermal simulation.

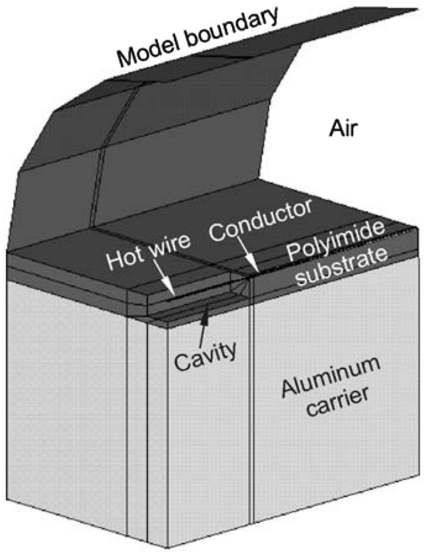

Fig. 10 Quarter-model of a MEMS wall hot-wire sensor with a cavity for electrothermal simulation.

on wire configuration, can amount to 15% of the hot-wire resistance, which could cause Joule heating within the conductors. To gain insight into the magnitude of these losses, three-dimensional simulations of wall hot-wire sensors featuring different hot-wire geometries are conducted. As stated before, cavity length is always equal to the hot-wire length simulated. Figure 10 depicts a typical quarter-model of a hot-wire sensor used for electrothermal three-dimensional FEM simulations.

A voltage drop across the hot wire and conducting path is modeled and Joule heating is calculated based on this information. Heat conduction from hot wire and conductor into the surrounding air and polyimide substrate is also simulated, yielding temperature distributions within and around the hot wire dependent on the selected geometry. Figure 11 depicts the temperature distribution in a model of a sensor featuring a hot wire of 800-μm length, 2-μm thickness, and 2-μm width, heated to an excess temperature of 200 K.

Simulated temperature distributions along the length of hot wires featuring different geometries and 2 mm of the conductor on the substrate are shown in Fig. 12. Cavity depth and width in these simulations are 100 and 400 μm, respectively. Hot-wire geometries were selected to investigate the influence of wire width and wire length on thermal losses into the conductors. Wire lengths of 400, 800, 1000, and 2000 μm are simulated in combination with wire widths of 2 and 5 μm. Wire thickness is kept constant at 2 μm. The selection of hot-wire width and thickness is partly driven by MEMS processing restrictions and considerations regarding the mechanical stability of the wires. In MEMS processing, a feature size of 2 μm is close to the lower limit achievable with optical contact lithography, whereas a layer thickness larger than 2 μm is not efficiently realizable by plasma-assisted deposition. Wires thinner than 2 μm, however, are prone to breakage during processing and usage.

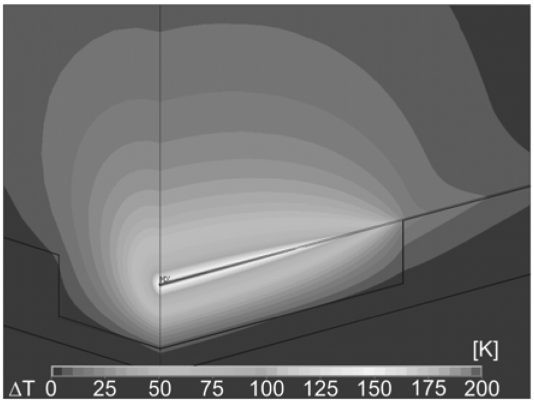

Fig. 11 Simulated temperature distribution around a wall hot wire on polyimide substrate with a cavity.

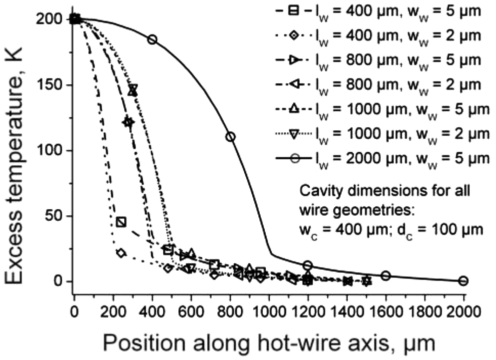

Fig. 12 Simulated temperature profiles along wall hot wires of various geometries.

Investigating the temperature profiles shown in Fig. 12, it is found that with constant hot-wire width and increasing hot-wire length, the temperature at the transition from wire to conductor and the overall temperature in the conductor are reduced. A reduction in temperature at the transition and in the conductor is also achieved by reducing wire width while keeping the wire length constant. Because the temperature within the conductor drops to ambient in all simulations, even though thermal boundary conditions do not enforce this behavior, Joule heating within the conductors can obviously be neglected. The increased temperature in parts of the conducting paths thus originates from the hot wire and is caused by conduction of heat. To minimize heat conduction from the hot wire into the conducting paths, and thus to reduce so-called thermal end losses, the hot wire should be long and narrow [26]. The two dominant parameters, hot-wire length and hot-wire width, can be combined to provide the length-to-width ratio of the hot wire, defined as l_W divided by w_W. As indicated in Fig. 12, the length-to-width ratio primarily determines heat losses into the conductors. Increasing the length-to-width ratio from 80 (which is associated with an excess temperature at the transition from hot wire to conductor of more than 50 K) to 200, the excess temperature, dependent on wire geometry, is reduced to 25 K ($l_W = 400\ \mu$m and $w_W = 2\ \mu$m) and 28 K ($l_W = 1000\ \mu$m and $w_W = 5\ \mu$m). A further increase of the length-to-width ratio to 400 is associated with wire-geometry-dependent excess temperatures of 19 K ($l_W = 800\ \mu$m and $w_W = 2\ \mu$m) and 21 K ($l_W = 2000\ \mu$m and $w_W = 5\ \mu$m).

The results obtained by two- and three-dimensional simulations indicate that a wall hot-wire sensor of the type schematically depicted in Fig. 3 featuring a hot wire of high length-to-width ratio on a 125-μm-thick polyimide substrate spanning a 100-μm-deep and 400-μm-wide cavity will exhibit the lowest thermal losses of all configurations examined. Additional constructive measures (e.g., covering the conducting paths or supporting the hot wire mechanically) would unavoidably yield higher thermal losses, because the thermal conductivity of all materials additionally introduced into the system would be substantially higher than the one of air.

D. Fabrication

Manufacturing of the sensors described is conducted using MEMS processing technology. To be able to process a flexible substrate material in equipment designed for handling of rigid silicon wafers, the polyimide foil is attached to a 2-mm-thick wafer. The adhesive employed is a solvent-free thermoplastic, which provides high bond strength after being heated and subjected to high pressure in a vacuum press during bonding [27]. Using this specific adhesive is necessary to prevent outgassing of solvents in high-vacuum environments common in MEMS processing. The uncoated foil (Fig. 13a) is placed in a sputtering machine, in which a 2-μm-thick nickel layer and a 200-μm-thick gold layer are deposited onto the top surface of the foil (Fig. 13b). To improve the adhesion of the nickel layer to the polyimide foil, high-vacuum plasma pretreatment including ion bombardment and exposure to reactive oxygen species is conducted. For structuring of the gold (Fig. 13c) and nickel (Fig. 13d) layers, two subsequent photolithography and wet-chemical-etching steps are carried out. A photoresist is spun on the metal layer to be etched and is structured by local exposure to light of a specific wavelength and subsequent removal of exposed resist using a developer solution. Etching of the gold layer employing a specific wet-chemical etchant provides a thin gold cover on top of the nickel bond pads and conductors. This gold cover passivates the nickel and provides a surface suited for gold wire bonding or soldering. By structuring of nickel using lithography and wet-chemical etching, the sensor structure comprising bond pads, conductors, and hot wire is established. To realize the cavity underneath the hot wire, an additional layer of metal is deposited onto the surface of the foil and the sensor structure by sputtering (Fig. 13e). This metal layer serves to protect the polyimide from etch attack during the following reactive-ion etching. The metal is removed locally by lithography and wet-chemical etching to uncover the polyimide around the hot wire (Fig. 13f). A RIE process optimized to provide both high etch rate and low surface roughness [22] is employed to etch a cavity of 100 μm into the polyimide (Fig. 13g). After RIE, the metal hard mask is removed by a combination of dry and wet etching, yielding a successfully manufactured single wall hot wire (Fig. 13h). Because MEMS technology allows for parallel processing, over 50 sensors are realized on a foil with a diameter of 100 mm in one process run. MEMS processing also allows for sensors of various cavity and wire geometries to be manufactured on one substrate simultaneously.

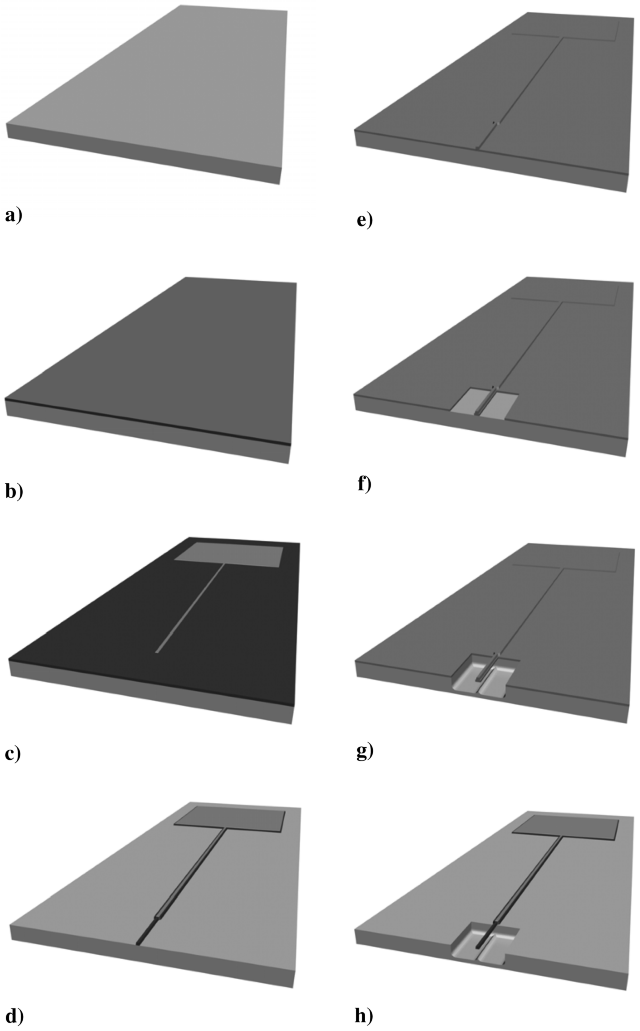

Fig. 13 Process flow for manufacturing of MEMS wall hot wires.

E. Sensor Types

According to results of the thermal simulations presented herein, optimized wall hot-wire sensors should feature a thick polyimide substrate carrying a hot wire of high length-to-width ratio spanning a sufficiently deep and wide air-filled cavity without mechanical supports. Further constraints on sensor design accrue from MEMS production techniques, requirements on mechanical stability and electrical properties of the hot wire, and limited commercial availability of potential sensor materials. Uncoated polyimide foils are typically available in thicknesses ranging from 25 to 125 μm. To optimize the thermal performance of the sensors, the thickest type is selected, which is sufficiently flexible to fit typical aerodynamic surfaces. In line with results from two-dimensional thermal simulations featuring a polyimide-substrate thickness of 125 μm, cavity depth and width are selected to be 100 and 400 μm, respectively. As noted previously, minimal hot-wire width and

Table 1 Calculated electrical resistance of hot wires of various geometries

	w_W	
l_W	2 μm	5 μm
400 μm	6.91 Ω	2.76 Ω
800 μm	13.82 Ω	5.58 Ω
1000 μm	17.28 Ω	6.91 Ω
2000 μm	34.55 Ω	13.82 Ω

Table 2 Different wire and cavity geometries based on an optimized basic sensor setup

	Geometry						
Type	w_W, μm	l_W, μm[a]	l_W/w_W	t_W, μm	w_C, μm	l_C, μm[a]	d_C, μm
A	2	800	400	2	400	800	100
B	5	2000	400	2	400	2000	100
C	2	400	200	2	400	400	100
D	5	1000	200	2	400	1000	100
E	2	800	400	2	1000	800	100
F	2/4/6; Ø3.75[b]	800	213.33	2	400	800	100

[a] The cavity length and the wire length are always equal.

[b] The type F hot wire features a tapered wire width increasing to the center of the wire in two steps (at 150 and 300 μm; compare Fig. 14).

maximal hot-wire thickness are limited to approximately 2 μm due to MEMS processing constraints. The mechanical stability of the hot wires is governed by their overall dimensions, with a small wire length and large wire width and thickness reducing the probability of breakage during processing or usage. As discussed in Sec. II.C, large wire lengths and small wire cross sections are necessary to reduce thermal end losses. To guarantee some mechanical stability, hot-wire thickness is set to 2 μm. The factor effectively limiting maximal hot-wire length and minimal hot-wire width, however, is not mechanical stability, but electrical resistance of the hot wire. Based on an electrical resistivity of thin-film nickel of 6.91×10^{-8} Ωm [24], Table 1 lists the electrical resistance of hot wires of various geometries at 293 K.

Electrical hot-wire resistance is critical because control circuits of conventional constant-temperature hot-wire anemometers, with which the MEMS wall hot wires should be compatible, are designed and optimized for a typical hot-wire cold resistance between 3 and 10 Ω. It was observed by the authors that a hot-wire cold resistance of more than 15 Ω is likely to cause problems when adjusting and optimizing the hot-wire time response on such systems. Additionally, the custom-made anemometer control circuits built to allow for more than 20 hot wires to be operated in parallel limit the maximal preset hot-wire resistance. To be able to achieve an overheat ratio of 2, the MEMS wall hot wires to be realized should exhibit a resistance smaller than 16.5 Ω.

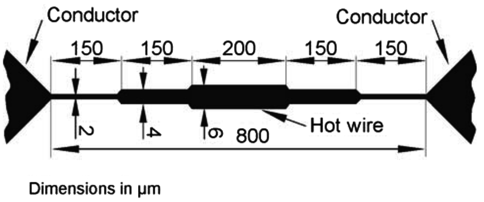

Fig. 14 Sketch of the top-view geometry of a hot wire of type F (not to scale).

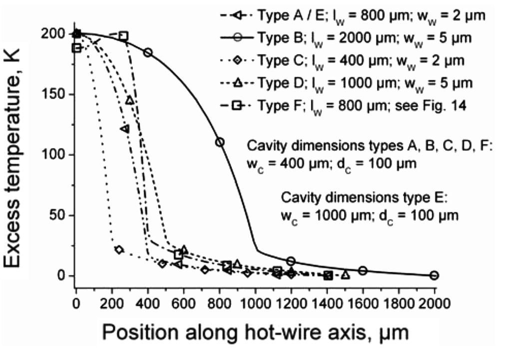

Fig. 15 Simulated temperature profiles of wall hot wires listed in Table 2.

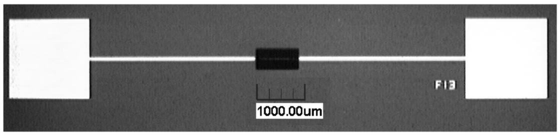

Fig. 16 Photograph of a MEMS wall hot-wire sensor on polyimide foil.

Based on these considerations and excluding hot-wire geometries that show a simulated excess temperature larger than 30 K at the transition from hot wire to substrate (compare Fig. 12) because of high thermal end losses, four different sensor configurations remain, which are described in the first four entries in Table 2 (sensor types A, B, C, and D).

Table 2 lists all sensor configurations selected for fabrication. Sensor types featuring a wire width of 5 μm (types B and D) are included to compensate for possible losses in yield of type A and C sensors due to processing difficulties and reduced mechanical stability. To verify the simulation-based conclusion that cavity width has a small influence on sensor power consumption at sufficiently large cavity depths (compare Figs. 7–9), a sensor type featuring a 1000-μm-wide cavity (type E) is chosen to be manufactured along with the four base configurations (types A, B ,C, and D). Because MEMS processing provides the unique possibility of realizing a hot wire with tapered wire width, the type F sensor was included. The design of the type F hot wire, as depicted in Fig. 14, is chosen to yield a more homogenous temperature distribution along the hot wire than predicted for the other sensor types.

The simulated temperature distributions along the length of all types of hot wires selected for fabrication are depicted in Fig. 15.

According to Table 2, hot-wire length-to-width ratios between 200 and 400 are best suited to fulfill the requirements stated previously. This conclusion is consistent with results of previous investigations on hot-wire length-to-diameter ratios, which found that the length-to-diameter ratio of a conventional hot wire should be between 200 and 400 for best performance [28].

Figure 16 depicts a successfully realized sensor of type F.

III. Experimental Setup

A. Temperature Coefficient of Resistance

Because an experimental determination of the temperature of a hot wire when heated by electrical power is very difficult, a temperature test cabinet is used to impose known temperatures onto the nickel thin-film hot wires to evaluate their TCR. Four-point probe measurement is used to precisely determine hot-wire resistance at various temperatures, as described in [21].

B. Static Calibration, Power Consumption, and Angular Measurement

Calibration and angular measurements are conducted in constant-temperature mode using an IFA 100 Anemometry System (TSI). No subsequent amplifying of hot-wire signals is conducted. Three single sensors glued onto a cylindrical adapter (Fig. 17) inserted flush with the surface of a flat plate are mounted in an open low-speed wind tunnel and evaluated simultaneously. Electrical contact is established using thin insulated wires soldered to the bond pads of the hot wires and led to the backside of the adapters through holes to the left and right of the individual sensor.

Freestream velocities from 0 to 20 m/s are used for static calibration of the sensors. A conventional wall shear stress balance mounted at the same distance from the leading edge of the flat plate as the sensors provides a reference wall shear stress signal. Resulting mean wall shear stresses range from 0 to approximately 1 $\mathrm{N/m^2}$. Calibration at overheat ratios of 1.2 and 1.8 is conducted in enforced turbulent flow. Anemometer output voltage and the voltage drop over the hot wire are recorded using a 16-bit analog-to-digital converter with a sampling rate of 15 kHz. Anemometer and hot-wire signals provided are averaged over 3 s to obtain reliable mean values. Hot-wire average voltage is used to determine the power consumption of the sensors. No signal processing to separate mean and fluctuating components of the output signals was conducted. Sensors without a cavity featuring the wire geometry of type A sensors are mounted on two of the three cylindrical adapters to obtain reference measurements for calibration and angular sensitivity.

Determination of the angular behavior of the hot wires is conducted by rotating the cylindrical adapter in the plane of the flat plate in steps of 15 deg. Thus, unfortunately the soldering areas are rotated into the flow upstream of the wires and are expected to be a source of flow disturbance at rotational angles around ±90 deg.

C. Cutoff-Frequency Measurement

In accordance with the measurement method proposed by Freymuth [29], an electrical sine sweep is fed into the hot-wire input circuit and compared with the response of the anemometer system. The generation of the sine sweep signal and the signal comparison are conducted using a signal generator and analyzer, and the output of the analyzer is postprocessed on a conventional personal computer.

IV. Results and Discussion

A. Temperature Coefficient of Resistance

The average TCR in a temperature range of 20 to 150°C of the nickel thin-film hot wires manufactured is 0.0053 $\mathrm{K^{-1}}$ and thus not substantially smaller than the one of a nickel reference resistance of 0.006 $\mathrm{K^{-1}}$. The resistance-temperature behavior of hot wire and reference resistor with a resistance of 14 Ω at 20°C is depicted in Fig. 18.

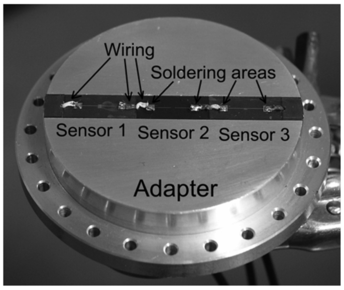

Fig. 17 MEMS wall hot-wire sensors of different geometries on a cylindrical carrier.

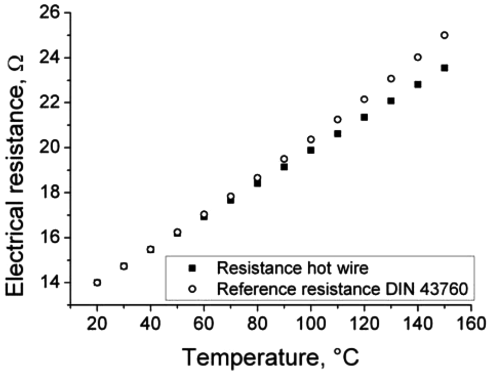

Fig. 18 Resistance-temperature behavior of nickel thin-film hot wire and reference resistance.

B. Static Calibration, Power Consumption, and Angular Measurement

Freestream velocities of 30 m/s inducing a wall shear stress of 2 $\mathrm{N/m^2}$ (as measured with a conventional wall shear stress balance) caused none of the hot wires to fail mechanically at overheat ratios of up to 1.8. It is expected that even substantially higher wall shear stresses will not cause mechanical failure of the sensors. Sensor calibration against the signal of a wall shear stress balance was conducted for all sensor geometries listed in Table 2.

Figure 19 shows calibration curves of sensor types B, C, D, E, and F and of a reference sensor without a cavity in a wall shear stress range from 0 to almost 1 $\mathrm{N/m^2}$ at an overheat ratio of 1.2 (left) and 1.8 (right). Data of sensor A were omitted in the graphs for improved clarity, because calibration curves of sensors of type A and type E show a maximum deviation of 5%. The ordinate of Fig. 19 displays the change in anemometer output voltage as a result of a change in wall shear stress, the values of which are provided on the abscissa. This graph allows one to easily compare the sensitivity S_τ, which is defined as the change in anemometer output voltage divided by the change in wall shear stress that caused the output signal change, of the different types of wall hot-wire sensors. The reference sensor without a cavity features the lowest average wall shear stress sensitivity of 0.027 $\mathrm{V/(N/m^2)}$ and 0.047 $\mathrm{V/(N/m^2)}$ in the given measurement range for overheat ratios of 1.2 and 1.8, respectively. Of all sensor types with a cavity, the sensor of type B, having the largest wire dimensions ($2000 \times 5 \times 2$ μm), shows the highest wall shear stress sensitivity of 0.095 $\mathrm{V/(N/m^2)}$ and 0.196 $\mathrm{V/(N/m^2)}$ at overheat ratios of 1.2 and 1.8, respectively. Only comparing sensors with equal hot-wire width (type B vs type D and type E vs type C) at both overheat ratios investigated, it is found that hot wires with a length-to-width ratio of 400 (type B and type E) feature larger wall shear stress sensitivities than sensor types with a length-to-width ratio of 200 (type D and type C). Within a group of hot wires with the same length-to-width ratio (type B vs type E and type D vs type C), those sensors featuring wider wires (type B and type D) exhibit a

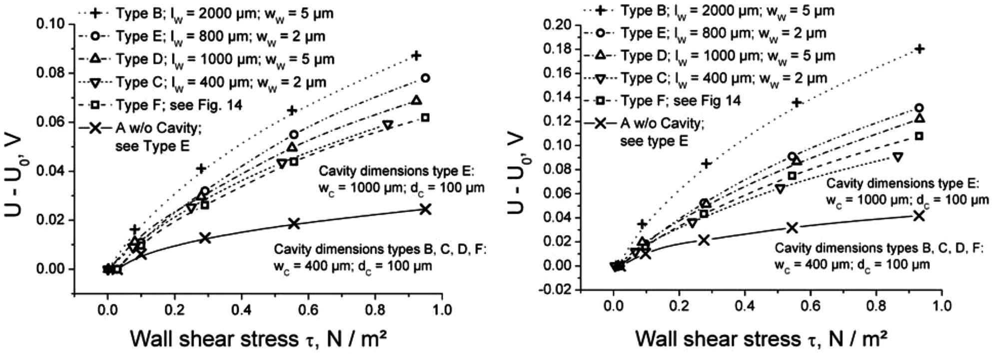

Fig. 19 Static calibration of MEMS wall hot wires; left: $a_W = 1.2$ and right: $a_W = 1.8$.

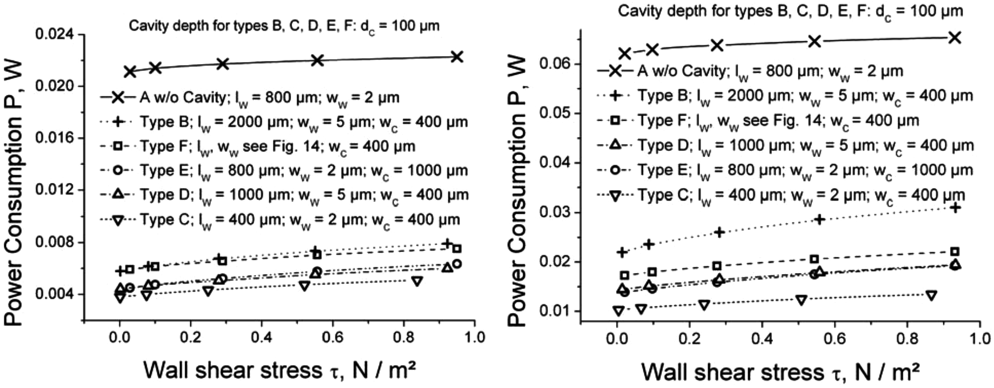

Fig. 20 Power consumption of MEMS wall hot wires; left: $a_W = 1.2$ and right: $a_W = 1.8$.

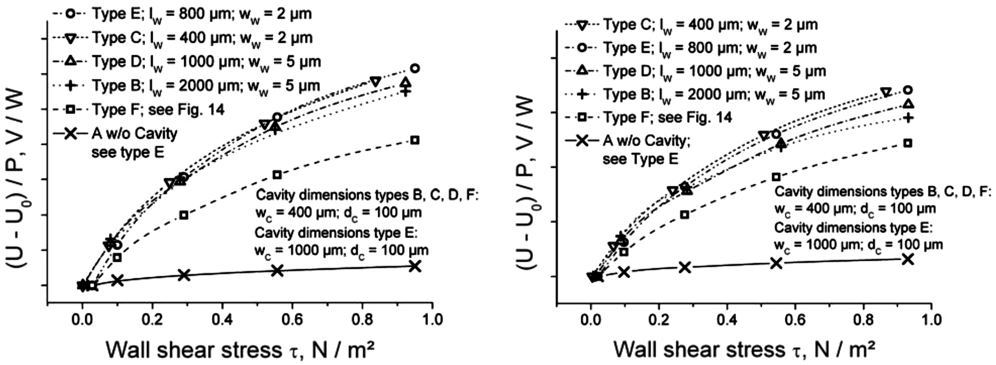

Fig. 21 Relative sensitivity of MEMS wall hot wires; left: $a_W = 1.2$ and right: $a_W = 1.8$.

higher wall shear stress sensitivity. This higher wall shear stress sensitivity, however, is connected to a higher power consumption of sensors with wider wires and wires with larger length-to-width ratios (Fig. 20). Only the sensor of type F featuring a hot wire with tapered cross section does not seem to fit into the observed correlation. Even though the sensor has a high power consumption, the sensitivity obtained is small compared with other sensor types with a cavity. This deviation is due to two facts: First, the average wire width of a hot wire of type F is 3.75 μm; consequently, the power consumption is higher than that of a 2-μm-wide hot wire. Second, based on this average wire width, a sensor of type F features an unfavorable length-to-width ratio of 213 (which, as already described, goes along with a reduced sensitivity). These two investigations well explain why this type of sensor does not exhibit a substantially higher wall shear stress sensitivity, but a significantly higher power consumption than a sensor of type C.

Normalizing the anemometer output voltage difference by the power consumption of each sensor, a relative sensitivity can be established, which is depicted in Fig. 21. Power normalized sensitivity, which is especially important when operating a multitude of sensors in an array setup, is highest for sensor types featuring 2-μm-wide hot wires. This observation confirms the results of the thermal simulations, which predict a lower excess temperature at the transition from hot wire to conductor and thus a better thermal insulation for thin hot wires. Differences in length-to-width ratio of the hot wires seem to have no pronounced influence on relative sensitivity in the experiments conducted. As expected, the relative sensitivities of sensor type F and the reference sensor without a cavity are low.

The normalized angular response of a hot wire of type B to a full rotation of the cylindrical sensor carrier at an overheat ratio of 1.8 and a freestream flow velocity of 20 m/s is depicted in Fig. 22. Fluid flow normal to the wire length is defined as 0 deg, and positive angles describe rotation in a negative mathematical direction. As expected, the flow is disturbed at angles of −90, 90, and 270 deg, due to upstream soldering areas.

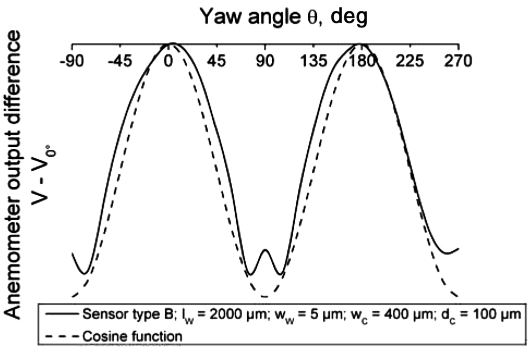

Fig. 22 Angular behavior of wall hot-wire sensor of type B and cosine function.

The simplest description of the effect of a flow approaching a hot wire at an angle not perpendicular to the wire length is given through the cosine law. The yaw angle (which, for conventional hot-wire probes is defined as the angle between the velocity vector and the vector normal to the wire with both lying in the plane of the support prongs) influences the effective cooling velocity as follows:

$$v_{\mathrm{eff}} = v_n = v \cdot \cos\theta$$

The cosine law states that only the velocity component normal to the hot wire contributes to sensor cooling [28]. Theoretically, this is only true for infinitely long hot wires, because these show no temperature variation along their length. It nevertheless has proven to be an excellent approximation for conventional hot wires with length-to-diameter ratios greater than 600 [30]. For hot wires of a smaller length-to-diameter ratio, the following equation has been proposed [31]:

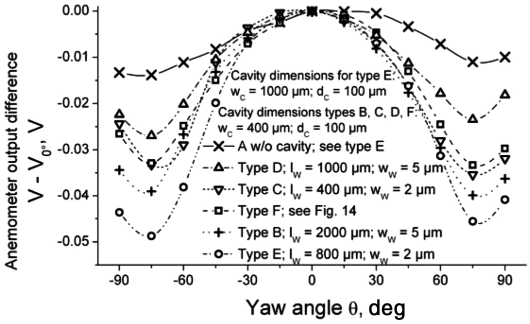

Fig. 23 Angular behavior of MEMS wall hot wires ($a_W = 1.2$ and $v_\infty = 20$ m/s).

$$v_{eff}^2 = v^2(\cos^2\theta + k^2 \cdot \sin^2\theta)$$

.

It was shown experimentally that the yaw factor increases with a decreasing hot-wire length-to-diameter ratio [30]. Thus, anemometer voltage will exhibit a sharper drop with an increasing yaw angle using hot wires with a higher length-to-diameter ratio, because the effective cooling velocity for such wires will be smaller. This conclusion is not only true for cylindrical hot wires, but has proven its qualitative validity for a probe-type MEMS hot-wire sensor with trapezoidal wire cross section [32]. Because the yaw factor is not only dependent on the hot-wire length-to-diameter ratio, but also on flow velocity and yaw angle itself [33], its determination is difficult and of very limited practical use. It nevertheless is of interest to check if the MEMS wall hot-wire sensors realized qualitatively behave according to theory. Yaw angle for wall hot-wire sensors is defined as the angle between the velocity vector and the vector normal to the wire, with both lying in a plane parallel to the surface of the sensor.

Comparing the yaw-angle dependent voltage output of a sensor of type B with the output predicted by the cosine law and ignoring the anomalies at −90, 90, and 270 deg caused by the experimental setup, some deviations (especially at around yaw angles of −45, 45, and 135 deg) can be observed. These deviations are in line with theory if a yaw factor larger than zero is assumed due to the length-to-width ratio of the hot wire of 400.

The sensitivity of different hot-wire geometries to changes in yaw angle for a rotation from −90 to 90 deg is depicted in Fig. 23. Data of all hot wires exhibit the assembly related disturbance at angles of −90 and 90 deg, which is also observed in Fig. 22. The signal of the reference sensor without a cavity shows the smallest dependence on the flow angle. This is caused by close thermal coupling of the wire and substrate generating a heated area on the sensor with a small effective length-to-width ratio, which is associated with a high yaw factor. Amongst the different types of wall hot-wire sensors with a cavity, the sensor types featuring a length-to-width ratio of 400 exhibit a larger drop of anemometer voltage when angled than hot wires with smaller length-to-width ratios. Such behavior is well in line with theory, because hot wires with larger length-to-width ratios normally exhibit smaller yaw factors. Comparing sensors with equal length-to-width ratios, 5-μm-wide hot wires are less sensitive to rotation than narrower types with an equal length-to-width ratio. It is assumed that the slightly more homogeneous temperature distribution and the reduced thermal losses to the conductors (compare Fig. 15) in narrower wires reduce cooling by the velocity component tangential to the wire and thus reduce the yaw angle factor. Because of the effective length-to-width ratio of 213, the sensor of type F should show a yaw-angle-dependent voltage drop comparable to that of a sensor of type C (2-μm-wide hot wire, length-to-width ratio of 200) and larger than that of a sensor of type D (5-μm-wide hot wire, length-to-width ratio of 200). The experimental data for a sensor of type F show a corresponding behavior.

The experimentally determined angular behavior of the different sensor types is qualitatively in line with results obtained from investigations on the yaw-angle dependence of conventional hot-wire probes. The results provided in Fig. 23 for single sensors can be used as the basis for yaw-angle detection using sensors mounted perpendicularly to each other. Such an arrangement can easily be realized using the hybrid arrays introduced in Sec. V.

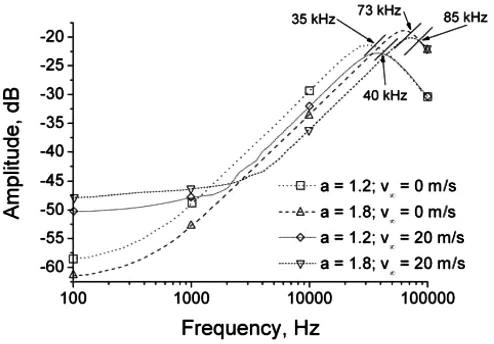

Fig. 24 Output amplitude of anemometer with type A sensor to electrical sine sweep.

C. Cutoff-Frequency Measurement

The cutoff frequency of a constant-temperature hot-wire anemometer system is a combination of the corresponding frequencies of the control electronics and the hot wire itself. Because the experimentally determined cutoff frequencies of the different MEMS wall hot wires examined only differ negligibly, a dominant influence of the control circuit on the cutoff frequency is assumed. The amplitude of the anemometer response to an electrical sine sweep is depicted in Fig. 24 for different flow speeds and overheat ratios for a sensor of type A.

V. Outlook: Realization of Arrays of MEMS Wall Hot Wires

To achieve both high temporal and spatial resolution for wall shear stress measurement on aerodynamic surfaces, the single sensors presented and experimentally characterized need to be organized to form an array. The design of such an array has to address the problem of electrically contacting individual sensors without compromising sensor density within the array. Flow disturbances close to the hot wires caused by wire contacting should be minimized and the mechanical flexibility of the single sensors should be retained. Array assembly should be flexible regarding the combination of different types of hot-wire sensors (types A to F, according to Table 2) to customize the array for specific applications.

All listed requirements are met by the setup presented in Fig. 25, which consists of a flex PCB made from thin FR4 material carrying the conductors and individual sensors glued onto the top surface. Because such assembly makes use of both circuit board and MEMS technologies, it is called a “hybrid array.” Figure 26 shows design and overall dimensions of the flex PCB carrier of the array.

Close spacing of individual hot-wire sensors within the array is rendered possible by realizing the conductors on the flex PCB and gluing the sensors onto conductors and circuit board with a 50-μm-thick double-sided adhesive tape. The pads on the left and right edges of the PCB are used for wire soldering. They are situated at a distance of at least 35 mm from all measurement locations to reduce flow

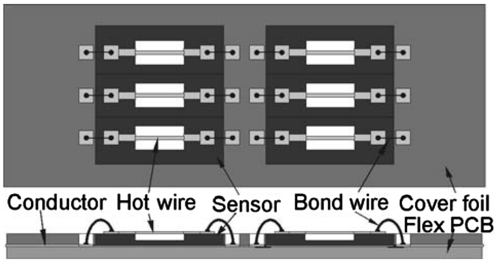

Fig. 25 Schematic of a hybrid-array arrangement of hot-wire sensors.

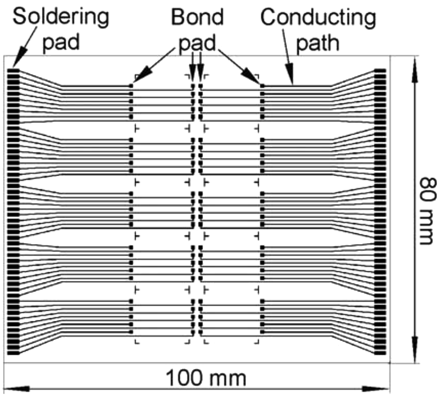

Fig. 26 Layout and overall dimensions of flex PCB for hybrid arrays.

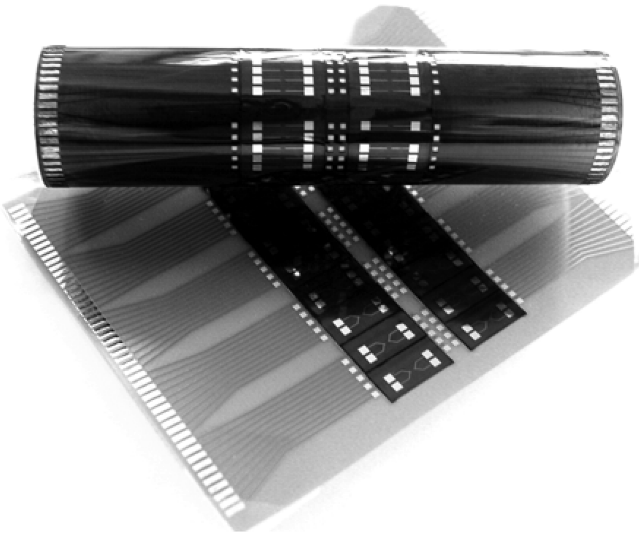

Fig. 27 Hybrid array with a cover foil on a cylinder; hybrid array on a flat plate.

disturbances. Electrical contact between individual hot-wire sensors and the square bond pads close to the center of the PCB is established by gold wire bonding. This contacting technology makes use of a 30-μm-thick gold wire, which is bonded to the pads by ultrasonically assisted welding. Thus, local flow disturbances are substantially reduced in comparison to wire-soldering techniques. Without further optimization of the setup, a hybrid array fitted to an aerodynamic surface exhibits two protruding edges upstream of the measurement locations, which influence the flow state considerably. The first protruding edge is due to the overall thickness of the hybrid array glued to the aerodynamic surface and can be avoided by milling a recess into the measurement surface to accommodate the array. The second step in height occurs because of the thickness of the polyimide substrate of the sensors. This step can be leveled off using a polyimide cover foil glued to the whole flex PCB. At sensor and pad positions, the cover foil is removed locally by laser cutting. Thus, a mostly uniform surface of the hybrid arrays is realized, which allows for flush mounting of the entire array onto the measurement surface. Figure 27 shows two hybrid arrays glued to different carriers for demonstration.

The manufacturing technologies presented in Sec. II.D could also be used to realize monolithic arrays of MEMS wall hot wires on polyimide foil with optimized wire and cavity geometries, as described in Secs. II.B and II.C. Aside from the need for a new set of lithographic masks, such monolithic arrays would suffer from low spatial density of sensors, due to the need to accommodate conductors and pads on the same surface as the sensors. Additionally, flow disturbances due to topside electrical contacts would still influence measurement results. To retain high sensor density and eliminate flow disturbances by wire bonding or soldering, electrical through-foil contacts need to be developed. Using such through-foil contacts to transfer the electrical signal from the top to the bottom side of the foil, the top side would be exclusively available for hot wires when conductors are placed on its bottom side. The realization of reliable through-foil contacts that do not compromise the mechanical flexibility of polyimide is a difficult task and the subject of future research.

VI. Conclusions

Different MEMS wall hot-wire sensors on a flexible substrate material were developed. Aerodynamic tests have proven the suitability of the sensors to accurately measure high-frequency fluctuations up to at least 73 kHz using standard constant-temperature anemometer systems. Based on FEM analysis and first principles, thermal optimization of the sensors was conducted, the effectiveness of which is well demonstrated by comparing the power consumption of hot-wire sensors with a cavity and hot-wire sensors without a cavity. Employing a flexible substrate material, a mismatch of measurement surface and sensor surface is avoided. Dependent on the individual application, a specific sensor type should be selected: If large absolute wall shear stress sensitivity is required and low power consumption is not of primary importance, a wire with a large cross section and length should be used. In applications requiring high energy efficiency, especially in array setups, sensors with a high power-related sensitivity seem best-suited. It was shown experimentally that MEMS wall hot wires with a small cross section provide high power-related wall shear stress sensitivity. Wires with a small length-to-width ratio but a large cross section should be used in flows in which wall shear stress components lateral to the wire of small but unknown magnitude could occur, because the flow-angle-dependent anemometer voltage drop is smallest for such sensors. When combining wall hot-wire sensors to build hybrid arrays for determination of flow direction and magnitude, sensors with a large length-to-width ratio and a small cross section are best suited due to their high yaw-angle sensitivity. The use of hybrid arrays is, however, not limited to yaw-angle determination. Such arrays exhibit a high sensor density and could be employed to monitor wall shear stress fluctuations with high temporal and spatial resolution, thus providing new insights into flow transition, separation, and other near-wall flow effects.

Acknowledgments

Financial support by the Deutsche Forschungsgemeinschaft (SFB 557, TP C6) is gratefully acknowledged. The authors would like to thank J. J. Czarnecki for providing valuable comments to improve the quality of the manuscript.

References

[1] Haritonidis, J. H., "The Measurement of Wall Shear Stress," *Advances in Fluid Mechanics Measurements*, edited by M. Gad-el-Hak, Lecture Notes in Engineering, Vol. 45, Springer, Berlin, 1989, pp. 229–262.

[2] Tsao, T., Jiang, F., Liu, C., Miller, R., Tung, S., Huang, J.-B., Gupta, B., Babcock, D., Lee, C., Tai, Y.-C., Ho, C.-M., Kim, J., and Goodman, R., "MEMS-Based Active Drag Reduction in Turbulent Boundary Layers," *Microengineering Aerospace Systems*, edited by H. Helvajian, Aerospace Press, El Segundo, TX, 1999, pp. 553–580.

[3] Gad-el-Hak, M., "Preface," *Flow Control*, Cambridge Univ. Press, New York, 2000, pp. 13–14.

[4] Sheplak, M., Padmanabhan, A., Schmidt, M. A., and Breuer, K. S., "Dynamic Calibration of a Shear-Stress Sensor Using Stokes-Layer Excitation," *AIAA Journal*, Vol. 39, No. 5, 2001, pp. 819–823; also AIAA Paper 98-0585, Jan. 1998.

[5] Chandrasekaran, V., Cain, A., Nishida, T., Cattafesta, L. N., and Sheplak, M., "Dynamic Calibration Technique for Thermal Shear-Stress Sensors with Mean Flow," *Experiments in Fluids*, Vol. 39, No. 1, 2005, pp. 56–65.

[6] Löfdahl, L., and Gad-el-Hak, M., "MEMS Applications in Turbulence and Flow Control," *Progress in Aerospace Sciences*, Vol. 35, No. 2, 1999, pp. 101–203.

[7] Burkhardt, O., Dinata, U., Warsop, C., and Nitsche, N., "New Developments in Surface Flow Sensor Technology Within the Framework of AEROMEMS," *Notes on Numerical Fluid Mechanics*, Vol. 76, No. 1, 2001, pp. 207–217.

[8] Sturzebecher, D., Anders, S., and Nitsche, W., "The Surface Hot Wire as a Means of Measuring Mean and Fluctuating Wall Shear Stress," *Experiments in Fluids*, Vol. 31, No. 3, 2001, pp. 294–301.

[9] Olson, S. D., and Thomas, F. O., "Quantitative Detection of Turbulent Reattachment Using a Surface Mounted Hot-Film Array," *Experiments in Fluids*, Vol. 37, No. 1, 2004, pp. 75–79.

[10] Desgeorges, O., Lee, T., and Kafyeke, F., "Calibration of Multiple Hot-Film Sensor Arrays and Skin Friction Measurement," *Experiments in Fluids*, Vol. 32, No. 1, 2002, pp. 37–43.

[11] Maluf, N., "The Sandbox: Materials for MEMS," *An Introduction to Microelectromechanical Systems Engineering*, Artech House, Boston, 2000, pp. 15–41.

[12] Jiang, F., Tai, Y.-C., Gupta, B., and Goodman, R., "A Surface-Micromachined Shear Stress Imager," *Proceedings of the Ninth IEEE Annual Workshop on Micro Electro Mechanical Systems*, Inst. of Electrical and Electronics Engineers, New York, 1996, pp. 110–115.

[13] Barth, P. W., Bernard, S. L., and Angell, J. B., "Monollithic Silicon Fabrication Technology for Flexible Circuit and Sensor Arrays," *Technical Digest of the IEEE Solid-State Sensor Conference*, Inst. of Electrical and Electronics Engineers, New York, 1984, pp. 40–41.

[14] Jiang, F., Walsh, K., Tsao, T., Tai, Y.-C., Lee, G. B., and Ho, C. H., "A Flexible MEMS Technology and Its First Application to Shear Stress Sensor Skins," *Proceedings of the Tenth International IEEE Workshop on MEMS (MEMS'97)*, Inst. of Electrical and Electronics Engineers, New York, 1997, pp. 465–470.

[15] Jiang, F., Tai, Y.-C., Huang, J.-B., and Ho, C. H., "Polysilicon Structures for Shear Stress Sensors," *Proceedings of the IEEE Region 10 International Conference on Microelectronics and VLSI (TENCON'95)*, Inst. of Electrical and Electronics Engineers, New York, 1995, pp. 12–15.

[16] Stephan, C. H., and Zanini, M., "A Micromachined, Silicon Mass-Air-Flow Sensor for Automotive Applications," *Transducers' 91: 1991 International Conference of Solid-State Sensors and Actuators*, Inst. of Electrical and Electronics Engineers, New York, 1991, pp. 30–33.

[17] Sugimoto, E., "Applications of Polyimide Films to the Electrical and Electronic Industries in Japan," *IEEE Electrical Insulation Magazine*, Vol. 5, No. 1, 1989, pp. 15–23.

[18] Morf, T., Biber, C., and Bachtold, W., "Effects of Epitaxial Lift-Off on the DC, RF, and Thermal Properties of MESFET's on Various Host Materials," *IEEE Transactions on Electron Devices*, Vol. 45, No. 7, 1998, pp. 1407–1413.

[19] Glassbrenner, C. J., and Slack, G. A., "Thermal Conductivity of Silicon and Germanium from 3°K to the Melting Point," *Physical Review*, Vol. 134, No. 4A, 1964, pp. A1058–A1069.

[20] Eriksson, P., Andersson, J. Y., and Stemme, G., "Thermal Characterization of Surface-Micromachined Silicon Nitride Membranes for Thermal Infrared Detectors," *Journal of Microelectromechanical Systems*, Vol. 6, No. 1, 1997, pp. 55–61.

[21] Sheplak, M., Chandrasekaran, V., Cain, A., Nishida, T., and Cattafesta, L. N., "Characterization of a Silicon-Micromachined Thermal Shear-Stress Sensor," *AIAA Journal*, Vol. 40, No. 6, 2002, pp. 1099–1104.

[22] Buder, U., von Klitzing, J.-P., and Obermeier, E., "Reactive Ion Etching for Bulk Structuring of Polyimide," *Sensors and Actuators A (Physical)*, Vol. 132, Nov. 2006, pp. 393–399.

[23] Huang, C., and Najafi, K., "Fabrication of Ultrathin p^{++} Silicon Microstructures Using Ion Implantation and Boron Etch-Stop," *Journal of Microelectromechanical Systems*, Vol. 10, No. 4, 2001, pp. 532–537.

[24] Reale, C., "Electrical Properties of Vacuum Deposited Nickel Films," *Physics Letters*, Vol. 24A, No. 3, 1967, pp. 145–146.

[25] Thun, R. E., Caudle, G. F., and Pasciutti, E. R., "Rugged Film Resistor Thermometer for the Measurement of Surface Temperatures," *Review of Scientific Instruments*, Vol. 31, No. 4, 1960, pp. 446–449.

[26] Bruun, H. H., "Basic Principles of Hot-Wire Anemometry," *Hot-Wire Anemometry*, 1st ed., Oxford Univ. Press, Oxford, 1995, pp. 19–70.

[27] Buder, U., Berns, A., von Klitzing, J.-P., Petz, R., Nitsche, W., and Obermeier, E., "AEROMEMS Wall Hot-Wire Anemometer on Polyimide Foil for Measurement of High Frequency Fluctuations," *Proceedings of the Fourth IEEE Conference on Sensors (IEEE Sensors 2005)*, Inst. of Electrical and Electronics Engineers, New York, 2005, pp. 545–548.

[28] Lomas, C. G., "Using the Heated Sensor Probe," *Fundamentals of Hot Wire Anemometry*, 1st ed., Cambridge Univ. Press, Cambridge, England, U.K., 1986, pp. 6–54.

[29] Freymuth, P., "Frequency Response and Electronic Testing for Constant-Temperature Hot-Wire Anemometers," *Journal of Physics E: Scientific Instruments*, Vol. 10, No. 7, 1977, pp. 705–710.

[30] Champagne, F. H., Sleicher, C. A., and Wehrmann, O. H., "Turbulence Measurements with Inclined Hot-Wires. Part 1: Heat Transfer Experiments with Inclined Hot-Wire," *Journal of Fluid Mechanics*, Vol. 28, No. 1, 1967, pp. 153–176.

[31] Hinze, J. O., *Turbulence*, 1st ed., McGraw–Hill, New York, 1959, p. 103.

[32] Jiang, F., Tai, Y.-C., Ho, C.-M., Karan, R., and Garstenauer, M., "Theoretical and Experimental Studies of Micromachined Hot-Wire Anemometers," *Technical Digest of the IEEE International Electron Devices Meeting 1994*, Inst. of Electrical and Electronics Engineers, New York, 1994, pp. 139–142.

[33] Jorgensen, F. E., "Directional Sensitivity of Wire and Fiber-Film Probes," *DISA Information*, Vol. 11, May 1971, pp. 31–37.

F. Coton
Associate Editor